

Characterization of Elastic Modulus Across the $(\text{Al}_{1-x}\text{Sc}_x)\text{N}$ System Using DFT and Substrate-Effect-Corrected Nanoindentation

Dong Wu, Yachao Chen, Sukriti Manna, Kevin Talley, Andriy Zakutayev^{ID}, Geoff L. Brennecka, Cristian V. Ciobanu, Paul Constantine, and Corinne E. Packard^{ID}

Abstract—Knowledge of accurate values of elastic modulus of $(\text{Al}_{1-x}\text{Sc}_x)\text{N}$ is required for design of piezoelectric resonators and related devices. Thin films of $(\text{Al}_{1-x}\text{Sc}_x)\text{N}$ across the entire composition space are deposited and characterized. Accuracy of modulus measurements is improved and quantified by removing the influence of substrate effects and by direct comparison of experimental results with density functional theory calculations. The 5%–30% Sc compositional range is of particular interest for piezoelectric applications and is covered at higher compositional resolution here than in previous work. The reduced elastic modulus is found to decrease by as much as 40% with increasing Sc concentration in the wurtzite phase according to both experimental and computational techniques, whereas Sc-rich rocksalt-structured films exhibit little variation in modulus with composition.

Index Terms—Aluminum nitride (AlN), elastic modulus, nanoindentation, scandium nitride, thin film.

I. INTRODUCTION

PIEZOELECTRIC aluminum nitride (AlN) thin films form the basis of surface acoustic wave and film bulk acoustic resonator (FBAR) devices that are widely used in telecommunications and other applications [1]–[6]. In the past decade, significant efforts have been directed at increasing the piezoelectric performance of AlN-based materials, largely via

Manuscript received February 11, 2018; accepted July 26, 2018. Date of publication August 16, 2018; date of current version November 7, 2018. This work was supported in part by the U.S. National Science Foundation under Grant DMREF-1534503 and in part by the U.S. Department of Energy, Office of Science, Office of Basic Energy Sciences through the Energy Frontier Research Center “Center for Next Generation of Materials by Design: Incorporating Metastability” under Contract DE-AC36-08GO28308 to NREL. (Corresponding author: Corinne E. Packard.)

D. Wu is with Lam Research, Wuhan 430075, China, and also with the Department of Metallurgical and Materials Engineering, Colorado School of Mines, Golden, CO 80401 USA.

Y. Chen, K. Talley, and G. L. Brennecka are with the Department of Metallurgical and Materials Engineering, Colorado School of Mines, Golden, CO 80401 USA.

S. Manna and C. V. Ciobanu are with the Department of Mechanical Engineering, Colorado School of Mines, Golden, CO 80401 USA.

A. Zakutayev is with the National Renewable Energy Laboratory, Golden, CO 80401 USA.

P. Constantine is with the Department of Computer Science, University of Colorado, Boulder, CO 80309 USA.

C. E. Packard is with the Department of Metallurgical and Materials Engineering, Colorado School of Mines, Golden, CO 80401 USA, and also with the National Renewable Energy Laboratory, Golden, CO 80401 USA (e-mail: cpackard@mines.edu).

Digital Object Identifier 10.1109/TUFFC.2018.2862240

Sc additions [6]–[12], which have been found to increase the longitudinal piezoelectric strain modulus d_{33} by up to 400% compared to pure AlN films for a Sc composition of 43% [9]. Computational studies suggest that such increases in $\text{Al}_{1-x}\text{Sc}_x\text{N}$ and related materials stem from mechanical softening of the wurtzite phase and may be associated in part with proximity to a phase boundary [13]–[16]. The elastic properties of these alloy systems are receiving less attention; experimental studies only minimally cover the range of 5%–30% Sc [17], [18], computational work does not extend beyond 50% Sc [13], [15], [19], and no previous study provides direct comparison between the computed and measured elastic constants.

In addition to being important from a fundamental standpoint, the elastic modulus is an essential property for FBARs and other devices because of its relation to mechanical resonance and role in energy dissipation and impedance matching. In resonator applications, one common figure of merit is the k^2Q product, where the mechanical quality factor Q is directly proportional to the stiffness with significant additional extrinsic contributions, and k^2 is the mode-appropriate electro-mechanical coupling coefficient. Moreover, while the most commonly experimentally measured and reported piezoelectric coefficient is the d tensor, which relates the electric field to strain or dielectric displacement to stress, first-principle calculations directly compute the e tensor, necessitating knowledge of the stiffness tensor in order to directly compare the measured d with the calculated d , e.g., $d_{33} = e_{33}/C_{33}^V$, where the V superscript indicates a condition of constant electric potential. Thus, the investigation of elastic properties is critical for evaluation of the functional performance of piezoelectric systems.

Various techniques are utilized to determine elastic modulus from thin films. The elastic modulus can be extracted from the resonance frequency of cantilever beams that are fabricated out of the thin film of interest [20]–[23], but this technique requires multiple film deposition, etching, and lithography procedures and optimization thereof. In contrast, instrumented indentation presents a nearly preparation-free testing method for thin films deposited on a substrate [18], [24]–[27], making it more suitable for rapid evaluation of elastic modulus in films fabricated via combinatorial deposition in order to cover a large composition range over a single sample library. However,

one important complication arises for testing thin films: when the size of the stress field induced by indentation approaches the film thickness, the measurement of the reduced elastic modulus is invariably influenced by the substrate. Recently, these limitations have been overcome by Li and Vlassak [28], who introduced a numerical calculation method based on an analytical model of the contact mechanics of a laminated film [29], showing that the impact of the substrate could be effectively removed from the data for a wide range of elastic dissimilarities and film thicknesses.

In this study, the reduced elastic moduli of $(\text{Al}_{1-x}\text{Sc}_x)\text{N}$ films are measured using a dynamic indentation technique. Accuracy of measurements is improved and quantified by removing the influence of substrate effects and by direct comparison of experimental results with density functional theory (DFT) calculations. This work covers the entire composition space in this system and maps elastic modulus with higher compositional resolution than previous studies, particularly over the 5%–30% Sc composition space that is of great application interest. The influences of composition and phase content on the elastic modulus of this nitride alloy are evaluated and discussed.

II. METHODS OF PREPARATION, CHARACTERIZATION, AND THEORETICAL ANALYSIS

Combinatorial $(\text{Al}_{1-x}\text{Sc}_x)\text{N}$ thin-film libraries are prepared through a magnetically enhanced RF reactive co-sputtering technique. The deposition is performed in a high-vacuum chamber with a base pressure $<1 \times 10^{-7}$ torr and process pressure of 2 mtorr at flows of 6-sccm Ar and 3-sccm N_2 . The deposition system is described in [30]. Fused silica (GM Associates) or Si(100) wafer (universitywafer.com) substrates of $51 \times 51 \text{ mm}^2$ size are mounted on a substrate stage equipped with a heater, and the temperature of the substrate is maintained at $400 \text{ }^\circ\text{C}$ during deposition. Prior to deposition, substrates are cleaned by presputtering with O_2 followed by Ar (fused silica) or Ar alone (Si). Two separate elemental targets (99.995% pure metallic Al and 99.9995% pure metallic Sc), installed at 45° angles with respect to the substrate, generate a lateral composition gradient across the substrate. A nitrogen plasma source is used to introduce nitrogen of increased reactivity to the deposition environment. During deposition, a cryogenic shroud is used to reduce the partial pressure of water in the system and minimize oxygen contamination. Power for each of the targets and deposition time for each library were chosen based on the data from preliminary runs, weighing the need for simultaneously achieving high crystallinity, balanced sputter yields, and reasonable deposition rates [31]. On each substrate, a 2×11 grid of thin film samples is deposited through a shadow mask, referred to here as a “sample library.” Each sample on the library is $2 \text{ mm} \times 10 \text{ mm}$ in size, with the long axes perpendicular to a line connecting the two sputter targets. This bins the composition gradient across the sample library into 11 different compositions, each with a pair of sibling samples. The thickness of each sample is measured using contact profilometry. Deposition parameters and resulting film characteristics are summarized in Table II for each sample library.

TABLE I
PARAMETERS OF NUMERICAL CALCULATION TO REMOVE THE SUBSTRATE EFFECTS

Parameters	Value
$M_{s_Si(100)}$	172.6 GPa
$M_{s_SiO_2}$	74.1 GPa
ν_{Si}	0.22
ν_{SiO_2}	0.19
ν_{ScN}	0.19
ν_{AlN}	0.24
$\nu_{AlSc1-xN}$	$0.24x+0.19(1-x)$

The composition of each thin film sample on the library is determined using spatially resolved X-ray fluorescence with a FISCHERSCOPE X-RAY XUV 773 and associated analysis software. The analysis is calibrated to single-composition AlN and ScN films of known thickness to improve the accuracy of measurements. Spatially resolved X-ray diffraction (XRD) is utilized to determine the crystalline structure and the texture of the films. The diffraction pattern of each film sample is collected using a Bruker D8 diffractometer with a 2-D area detector and collimated $\text{CuK}\alpha$ radiation in a θ – 2θ configuration. The intensity counts collected by the detector are integrated across the chi dimension to provide an intensity versus 2θ pattern.

The stiffness of each sample on the library is measured using dynamic nanoindentation [32] on a TI-950 Hysitron Triboindenter instrument equipped with a Berkovich-geometry diamond indenter tip. The area function A of the Berkovich indenter tip is calibrated on fused silica. Four dynamic indentation tests with a peak load of 3 mN are performed on each film sample on the library, with an excitation frequency of 150 Hz and a constant strain rate of 0.06 s^{-1} . Analysis of nanoindentation data and correction to remove the substrate effects is conducted according to the method of Li and Vlassak [28]. Though Li and Vlassak’s method has been incorporated into a commercially available software package offered by Bruker, we have created our own implementation of the method, allowing for customization of optimization parameters and the utilization of parallel processing on a high-performance computing cluster. The values of material parameters used in the method are listed in Table I. Step sizes of 4 GPa and 0.1 are used to resolve substrate-effect-corrected elastic modulus of the film M_f and dimensionless plastic thinning parameter η respectively, for analysis of each set of indentation data. Each indentation test containing 61 data points in total is reduced to six data points uniformly spaced over the total indentation time to increase the speed of calculation. The error associated with using a reduced data set is found to be smaller than that associated with the (M_f, η) step sizes utilized here.

The Vienna *Ab initio* Simulation Package is used for structural optimizations (ionic positions and lattice parameters) and calculations of elastic constants of the $(\text{Al}_{1-x}\text{Sc}_x)\text{N}$ lattice, with projector augmented waves (PAW) in the generalized gradient approximation using the Perdew–Burke–Ernzerhof

TABLE II
FILM DEPOSITION PARAMETERS

Sample Library	Power Sc/Al (W)	Deposition time (min)	x% in $\text{Al}_{1-x}\text{Sc}_x\text{N}$	Thickness range (nm)
#1 film/ SiO_2	10/50	120	1.2 ~ 3.4	98 ~ 245
#2 film/ SiO_2	20/50	120	2.83 ~ 10.08	149 ~ 318
#3 film/ SiO_2	60/30	240	44 ~ 83.4	610 ~ 1046
#4 film/ SiO_2	50/0	270	100	138 ~ 298
#5 film/Si	15/60	240	1.78 ~ 6.38	382 ~ 779
#6 film/Si	30/60	240	7.93 ~ 25.08	468 ~ 875
#7 film/Si	60/60	240	19.33 ~ 51.37	603 ~ 970

(PBE) exchange-correlation functional [33]–[35]. In these calculations, plane-wave energy cutoffs of 540 eV and tolerances for total energy of 10^{-8} and 10^{-7} eV for electronic and ionic convergence are applied, respectively. The simulation supercells are constructed using special quasi-random structures (SQSs), allowing efficient simulations of random alloys using a small number of atoms [36]; five SQS structures are assembled and run for each alloy composition. For the wurtzite structure (B1), a 32-atom supercell ($2 \times 2 \times 2$ unit cells) with a $6 \times 6 \times 2$ Monkhorst-Pack k -point mesh is used to sample the Brillouin zone with their origins set at the Γ point, resulting in 40 irreducible k -points [37]. The calculations of scandium-rich rock salt structures (B4) are performed using a 64-atom supercell ($2 \times 2 \times 2$ unit cells), and Brillouin zones are sampled by $4 \times 4 \times 4$ Monkhorst-Pack meshes with their origins set at the Γ points (36 irreducible k -points). At the relaxed (equilibrium) values for the lattice parameters, the elastic constants are computed as second derivatives of the total energy density with respect to small strains applied to the supercells [38]. In particular, the independent elastic constants: C_{11} , C_{12} , C_{13} , C_{33} , and C_{44} for the hexagonal wurtzite structure, and C_{11} , C_{12} , and C_{44} for the cubic rock salt structure are determined from specific strain matrices [39].

III. RESULTS AND DISCUSSION

A. Thickness, Composition, and Microstructure of the $(\text{Al}_{1-x}\text{Sc}_x)\text{N}$ Films

Intentional gradients in film composition and thickness exist along the row direction of the thin film sample libraries because of the position of film samples with respect to the sputtering targets and can be modified by varying the power applied to the targets. Ranges of composition and thickness of the deposited films are provided in Table II; measured values vary continuously along the row direction of the film sample libraries.

The crystalline structure(s) and phase(s) of all samples are characterized using XRD. In Fig. 1, the collection of XRD patterns are represented with the film Sc content on the ordinate axis, the diffraction angle 2θ on the abscissa, and the color indicates the normalized diffraction intensity. For comparison to more typical diffraction plots having 2θ on the abscissa and diffraction intensity on the ordinate, line plots of this form are shown in white for the compositional extremes of

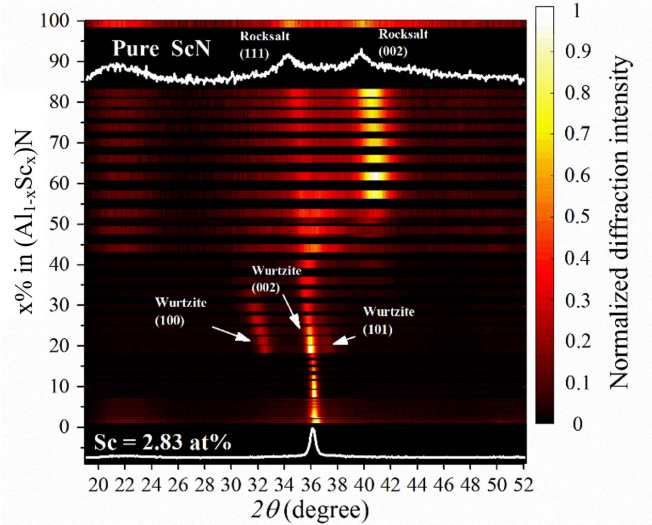


Fig. 1. A transition from wurtzite to rock salt structure is indicated by XRD patterns of the $(\text{Al}_{1-x}\text{Sc}_x)\text{N}$ film.

AlN (bottom) and ScN (top). The Lotgering factor is calculated to quantify the degree of (002) c -axis texture in a film, where 1 indicates a c -axis texture, and 0 indicates a randomly oriented film. [40]. Only one dominant diffraction peak, (002), is identified over the measured 2θ range in $(\text{Al}_{1-x}\text{Sc}_x)\text{N}$ samples below 19.3% (cation percent) Sc (#1 and #2) with a Lotgering factor of 1, indicating that the deposited $(\text{Al}_{1-x}\text{Sc}_x)\text{N}$ film has a wurtzite structure with a strong c -axis texture. For those film alloys with intermediate alloying concentration (19.3%–33.2% Sc) deposited on Si(100), wurtzite (100) and (101) peaks are present in addition to the (002) peak. Increasing the Sc concentration across this range leads to a gradual decrease in the Lotgering factor from 0.95 to 0.7, indicating a loss of strong c -axis texture in the films. For the sample library #3 with high Sc content, a coexistence of two crystalline phases consisting of hexagonal wurtzite and cubic rock salt structures are observed when the Sc content increases from 33.2% to 83.4%. The XRD pattern of the pure ScN film (#4) has only two diffraction peaks (111) and (002) in this 2θ range, consistent with untextured rock salt crystal structure.

It should also be noted that as the Sc content increases in materials of either structure, all diffraction peaks move to lower angle, as shown in Fig. 2. Our DFT calculations for equilibrium lattice constants as a function of Sc composition x show both wurtzite lattice parameters a and c increasing with increasing x , consistent with other studies in [14], [15], and [19]. Using the DFT lattice constants, we have calculated the 2θ locations of the XRD peaks and compared with those determined experimentally. The experimental and DFT results agree with each other across the entire composition range, albeit with the DFT results systematically underestimating the 2θ positions in experimental data due to the fact that the PBE functional [35] overestimates the experimental lattice constants by $\sim 1\%$ – 3% [41]. The shifting trend of diffraction peaks is ascribed to lattice expansion in the $(\text{Al}_{1-x}\text{Sc}_x)\text{N}$ system, as the Sc ion is larger than the Al ion with the ionic radius ratio of $\text{Sc}/\text{Al} = 1.39$ [42].

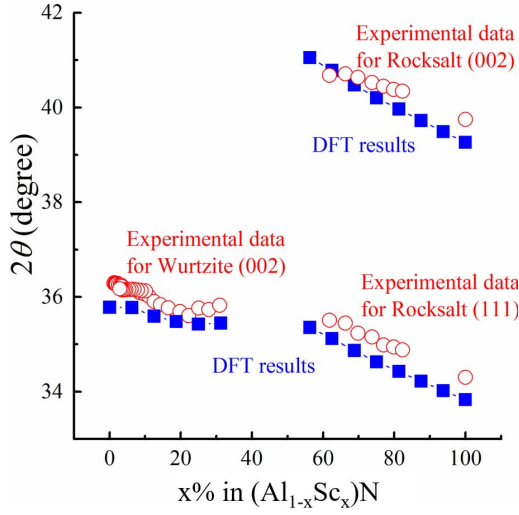


Fig. 2. Experimental and DFT-calculated positions of the main XRD peaks: wurtzite (002), and rock salt (002) and (111) for $(Al_{1-x}Sc_x)N$ structures as functions of Sc content x show shifts in positions as a result of lattice distortion due to alloying.

B. First-Principle Calculations of Elastic Constants and Polycrystalline Averages for $(Al_{1-x}Sc_x)N$ Films

The elements of the stiffness matrix for $(Al_{1-x}Sc_x)N$ in either the wurtzite or rock salt structure (depending upon x) are determined from total energy DFT calculations and are plotted in Fig. 3(a) as a function of Sc content. Relaxations of the computational SQS cells for Sc cation content $>50\%$ Sc lead to significant deviations from expected wurtzite parameters, so values are reported here for wurtzite-structured material for Sc contents $\leq 50\%$, and rock salt-structured material for Sc contents $\geq 50\%$. The values and trends shown in Fig. 3(a) are similar to those reported in [15] and [19], and reflect a decrease of the stiffness components C_{33} and C_{11} with Sc content x .

Despite other reports of elastic softening with increasing Sc concentration in wurtzite [15], direct comparisons with experimental data that do not independently access any of the stiffness constants can only be enabled by appropriate averaging of the elements of the stiffness tensor, C . The presence of texture in the polycrystalline wurtzite-structured $(Al_{1-x}Sc_x)N$ adds complexity to this analysis; however, it is reasonable to bound the elastic modulus between that of an isotropic medium of randomly oriented grains [43]–[45] and that of a fully c -axis oriented material that can be approximated as an orthotropic medium [46]. For the orthotropic bound, the indentation modulus M_{film} is calculated as

$$M_{\text{film}} = 2 \sqrt{\frac{C_{31}^2 - C_{13}^2}{C_{11}} \left/ \left(\frac{1}{C_{44}} + \frac{2}{C_{31} + C_{13}} \right) \right.} \quad (1)$$

where $C_{31} = \sqrt{C_{11}C_{33}}$. The indentation modulus for the isotropic bound is found from $M = 9BG/[(3B + G)(1 - \nu^2)]$, where ν is Poisson's ratio. For the wurtzite structure, the bulk modulus B and shear modulus G are estimated in terms of a Voigt approximation [47] and a Reuss approximation [48] for the upper and lower bounds of modulus values of hexagonal

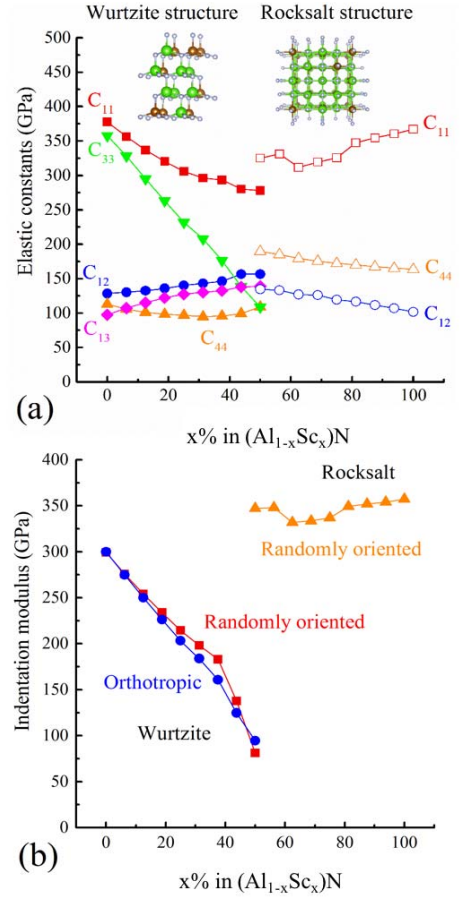


Fig. 3. Elastic constants of $(Al_{1-x}Sc_x)N$ with wurtzite structure (C_{11} , C_{12} , C_{33} , C_{44} , and C_{13}) or rock salt structure (C_{11} , C_{12} , and C_{44}) as a function of Sc content. (a) DFT results for single-crystal values. (b) Polycrystalline averages computed from the DFT single crystal results in the random (wurtzite and rock salt) and orthotropic (wurtzite) limits.

crystals, respectively. According to the Hill approximation[47] for polycrystalline materials, the effective moduli for isotropic media are written as the arithmetic mean of the two bounds: $B = (B_V + B_R)/2$ and $G = (G_V + G_R)/2$, where B_R , B_V , G_R , and G_V correspond to the Voigt and Reuss approximations and can be found in [44]. For the rock salt cubic structure, B is estimated as a linear combination of two elastic constants: $B = (C_{11} + 2C_{12})/3$, while G is averaged as: $G = (G_V + G_R)/2$, where $G_V = (C_{11} - C_{12} + 3C_{44})/5$ and $G_R = (5(C_{11} - C_{12})C_{44})/(4C_{44} + 3(C_{11} - C_{12}))$.

Fig. 3(b) shows the indentation modulus across the composition range, determined using the elements of the DFT-computed stiffness tensor C . The calculated indentation modulus of wurtzite $(Al_{1-x}Sc_x)N$ decreases with increasing Sc content, reaching as low as 81 GPa for a Sc content of 50 at%, while the relaxed unit cell maintains a wurtzite structure. Both isotropic and orthotropic assumptions of the crystalline microstructure are applied in calculating the indentation modulus, but no substantial difference is observed. This indicates that the softening of the wurtzite structure results in a drastic reduction in elastic modulus, regardless of the film texture. On the other hand, the calculated indentation modulus of rock salt $(Al_{1-x}Sc_x)N$ only changes slightly with Sc content

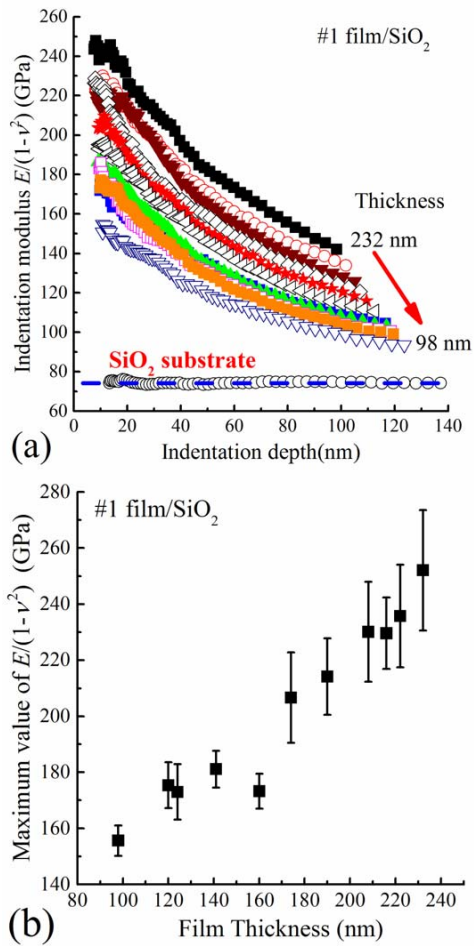


Fig. 4. Indentation modulus of the $(\text{Al}_{1-x}\text{Sc}_x)\text{N}/\text{SiO}_2$ system (a) as a function of indentation depth. (b) Maximum values of indentation modulus as a function of film thickness.

because the stiffness constants C_{11} , C_{12} , and C_{44} of the cubic rock salt are less sensitive to composition.

C. Elastic Response of Thin $(\text{Al}_{1-x}\text{Sc}_x)\text{N}$ Films on Substrates

The raw indentation data of library #1 are plotted as a function of indentation depth in Fig. 4(a). Each of the 11 data series (one from each sample of the library) is plotted, with uncorrected indentation modulus ($E/(1-\nu^2)$) as a function of indentation depth. In contrast to the depth-independent modulus of the SiO_2 substrate, which is determined to be 74.1 GPa, the indentation modulus of each film/substrate samples decreases sharply with increasing indentation depth. Given the same indentation depth, the indentation modulus increases with increased film thickness. Sample library #1 has only a very small variation in Sc content; thus, the variation of modulus is not attributable to compositional changes, but instead indicates impact from the compliant substrate. The maximum values of uncorrected indentation modulus for each indentation test occur at the lowest indentation depths and are plotted against film thickness in Fig. 4(b). With the exception of the thinnest film, the plotted modulus values are derived from measurements from less than 10% of total film thickness. Even though these values occur at shallow penetrations,

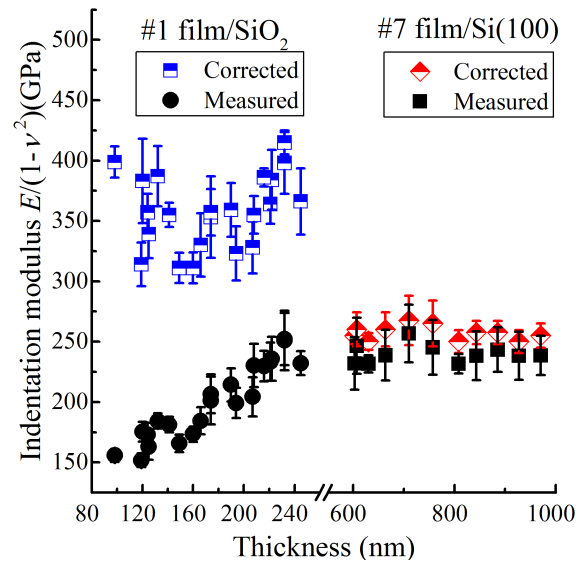


Fig. 5. Extraction of indentation modulus of representative film sample library: #1 $(\text{Al}_{1-x}\text{Sc}_x)\text{N}/\text{SiO}_2$ and #7 $(\text{Al}_{1-x}\text{Sc}_x)\text{N}/\text{Si}(100)$ following numerical calculation analysis.

where the influence of the substrate is minimized, the impact is obviously not negligible because uncorrected modulus varies over 100 GPa with only a 2.2% absolute variation in Sc content.

The indentation moduli of thin film samples are corrected to remove the impact of the substrate following the numerical procedure developed by Li and Vlassak [28]. For all film samples, the optimized η has a value of 0 because plasticity in the nitride film is limited. The values of indentation modulus with and without correction are shown for two sample libraries in Fig. 5. For the $(\text{Al}_{1-x}\text{Sc}_x)\text{N}$ thin film deposited on a compliant substrate (#1 film/ SiO_2), there is little variance in composition, so the apparent increase of indentation modulus with film thickness comes from a severe substrate effect. After correction, the moduli are shown to be approximately 350 GPa, within error of the 354 GPa reported in [26], and the dependence on film thickness has been eliminated. Corrections to remove the substrate effect increase the indentation modulus by 100–250 GPa. The measured indentation modulus of the thicker $(\text{Al}_{1-x}\text{Sc}_x)\text{N}$ film deposited on a stiffer substrate (#7 film/ $\text{Si}(100)$) does not depend strongly on film thickness, but still yields an increase of 15–20 GPa in the indentation modulus after correction. In this sample, the modulus mismatch between substrate and film is lower, and the indentation depth relative to total film thickness is substantially lower, leading to smaller corrections.

The indentation moduli of $(\text{Al}_{1-x}\text{Sc}_x)\text{N}$ films with varied Sc content are obtained, corrected, and evaluated for all films using the same procedure. Fig. 6 shows all of the data and plots modulus as a function of Sc content. Each data point represents the average of all four indentation results on each composition for each sample library, with error bars representing the standard deviation. It is often observed in AlN-based films that differences in films grown on different substrates are dominated by the residual stress state, and that

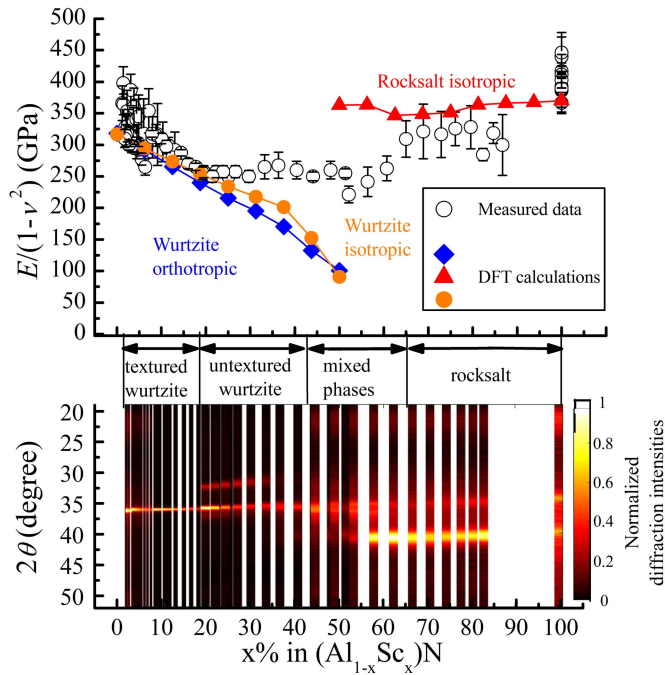


Fig. 6. Indentation modulus and XRD patterns of $(\text{Al}_{1-x}\text{Sc}_x)\text{N}$ as a function of Sc content. The deviation of experimental indentation modulus from theoretical prediction is consistent with the coexistence of two phases observed by XRD.

nucleation and microstructure development are similar across different substrates [49]–[54]. We found that cracks tended to occur more frequently in films on SiO_2 substrates, likely due to the thermal expansion coefficient mismatch between the substrate and film. Crack-free films are necessary for valid indentation measurements; thus, we discarded cracked films and instead used silicon substrates (with lower thermal expansion coefficient mismatch) for several libraries. Substrate-effect-corrected data from sample libraries #2 and #5, which cover a similar composition range but have different substrates, converge in a single trend, consistent with other studies that have seen negligible differences in AlN-based film growth on different substrates. In the modulus-composition diagram, the substrate-effect-corrected indentation modulus decreases with increasing Sc content from 0% to $\sim 25\%$. This result mirrors the trend observed in the work of Zywitzki *et al.* [17] and Žukauskaitė *et al.* [18], but maps the changes in indentation modulus with much higher compositional resolution. The values of indentation modulus obtained here are more similar to those of Zywitzki *et al.* [17] and are higher than those reported by Žukauskaitė *et al.* [18], who report restricting indentation depth to less than 10% of the film thickness but do not provide sufficient evidence that substrate compliance effects are avoided. We confirm that indentation modulus decreases monotonically with Sc addition between the sparse data provided by other reports. Furthermore, the substrate-effect-corrected indentation modulus is well-matched by estimations of the indentation modulus made from texture-based averaging of the DFT results in the range of 0%–25% Sc, showing that DFT calculations can provide accurate estimates of modulus which may aid in accelerating the discovery of

piezoelectric materials tailored to optimizing specific figures of merit. In addition, these combined experimental and computational findings support the idea that the oft-reported increase in piezoelectric strain response with Sc additions to AlN are driven at least as much by the reduction in material stiffness (as much as 40%, as shown here) as by the direct improvement in intrinsic electromechanical response (also $\sim 40\%$ change over the same composition space) [58], and highlight the need for further materials development for improved performance in resonator applications.

Between 25% and 65% Sc, the corrected indentation modulus stays roughly constant, consistent with the results from Zywitzki *et al.* [17] that covered the range of 30%–45% Sc. The discrepancy between the experimental and computed indentation modulus in this range is due to the mixture of phases in experiments (wurtzite and rock salt), whereas computations are carried out for either wurtzite or rock salt (not mixed); it is not tractable to have mixed phases in the DFT simulation cells. Above 65% Sc, a range which has not previously been experimentally or computationally explored, the films have rock salt structure and exhibit substrate-corrected indentation modulus values consistent with DFT calculations. Rock salt $(\text{Al}_{1-x}\text{Sc}_x)\text{N}$ exhibits little compositional variation in elastic modulus.

IV. CONCLUSION

Thin films of $(\text{Al}_{1-x}\text{Sc}_x)\text{N}$ across the entire composition space are deposited and characterized. In mapping elastic modulus across the full $(\text{Al}_{1-x}\text{Sc}_x)\text{N}$ system, we show that accuracy of measurements is improved and quantified by removing the influence of substrate effects and by direct comparison of experimental results with DFT calculations. The indentation modulus of $(\text{Al}_{1-x}\text{Sc}_x)\text{N}$ in the wurtzite phase decreases with increased Sc content, whereas the modulus is relatively insensitive to Sc content in the rock salt structure. The coexistence of hexagonal wurtzite and cubic rock salt structure occurs in nitride films with intermediate Sc content and is reflected in experimentally observed indentation modulus between that of the wurtzite and rock salt phases. This study reinforces the importance of reduced elastic modulus on the increased strain response of Sc-modified AlN piezoelectrics and has provided an efficient approach to evaluate the elastic modulus of a thin film on compliant substrate in a high-throughput manner.

ACKNOWLEDGMENT

The *Ab initio* calculations were performed using computational resources sponsored by the Department of Energy’s Office of Energy Efficiency and Renewable Energy and located at the National Renewable Energy Laboratory (NREL), Golden, CO, USA. The Numerical Computations were carried out with NREL facilities and with the Colorado School of Mines High Performance Computing Resources. The use of combinatorial thin film synthesis and spatially resolved characterization facilities at NREL as a part of the High Throughput Experimental Materials Collaboratory is gratefully acknowledged.

REFERENCES

- [1] M. Clement, L. Vergara, J. Sangrador, E. Iborra, and A. Sanz-Hervás, "SAW characteristics of AlN films sputtered on silicon substrates," *Ultrasonics*, vol. 42, nos. 1–9, pp. 403–407, Apr. 2004.
- [2] M. A. Odintzov, N. I. Sushentzov, and T. L. Kudryavtzev, "AlN films for SAW sensors," *Sens. Actuators A, Phys.*, vol. 28, no. 3, pp. 203–206, 1991.
- [3] T. Palacios *et al.*, "Nanotechnology for SAW devices on AlN epilayers," *Mater. Sci. Eng. B*, vol. 93, nos. 1–3, pp. 154–158, 2002.
- [4] K. Tonisch, V. Cimalla, C. Foerster, H. Romanus, O. Ambacher, and D. Dontsov, "Piezoelectric properties of polycrystalline AlN thin films for MEMS application," *Sens. Actuators A, Phys.*, vol. 132, no. 2, pp. 658–663, 2006.
- [5] G. Piazza, V. Felmetger, P. Muralt, R. H. Olsson, III, and R. Ruby, "Piezoelectric aluminum nitride thin films for microelectromechanical systems," *MRS Bull.*, vol. 37, no. 11, pp. 1051–1061, Nov. 2012.
- [6] A. Žukauskaitė *et al.*, "Microstructure and dielectric properties of piezoelectric magnetron sputtered $\text{w-Sc}_x\text{Al}_{1-x}\text{N}$ thin films," *J. Appl. Phys.*, vol. 111, no. 9, p. 093527, 2012.
- [7] P. M. Mayrhofer *et al.*, "Microstructure and piezoelectric response of $\text{Y}_x\text{Al}_{1-x}\text{N}$ thin films," *Acta Mater.*, vol. 100, pp. 81–89, Nov. 2015.
- [8] P. M. Mayrhofer, H. Euchner, A. Bittner, and U. Schmid, "Circular test structure for the determination of piezoelectric constants of $\text{Sc}_x\text{Al}_{1-x}\text{N}$ thin films applying laser Doppler vibrometry and FEM simulations," *Sens. Actuators A, Phys.*, vol. 222, pp. 301–308, Feb. 2015.
- [9] M. Akiyama, T. Kamohara, K. Kano, A. Teshigahara, Y. Takeuchi, and N. Kawahara, "Enhancement of piezoelectric response in scandium aluminum nitride alloy thin films prepared by dual reactive cosputtering," *Adv. Mater.*, vol. 21, no. 5, pp. 593–596, Feb. 2009.
- [10] M. Akiyama, K. Kano, and A. Teshigahara, "Influence of growth temperature and scandium concentration on piezoelectric response of scandium aluminum nitride alloy thin films," *Appl. Phys. Lett.*, vol. 95, no. 16, p. 162107, 2009.
- [11] T. Yokoyama, Y. Iwazaki, Y. Onda, T. Nishihara, Y. Sasajima, and M. Ueda, "Effect of Mg and Zr co-doping on piezoelectric AlN thin films for bulk acoustic wave resonators," *IEEE Trans. Ultrason., Ferroelectr., Freq. Control*, vol. 61, no. 8, pp. 1322–1328, Aug. 2014.
- [12] Y. Iwazaki, T. Yokoyama, T. Nishihara, and M. Ueda, "Highly enhanced piezoelectric property of co-doped AlN," *Appl. Phys. Express*, vol. 8, no. 6, p. 061501, 2015.
- [13] C. Tholander *et al.*, "Ab initio calculations and experimental study of piezoelectric $\text{Y}_x\text{In}_{1-x}\text{N}$ thin films deposited using reactive magnetron sputter epitaxy," *Acta Mater.*, vol. 105, pp. 199–206, Feb. 2016.
- [14] C. Höglund *et al.*, "Wurtzite structure $\text{Sc}_{1-x}\text{Al}_x\text{N}$ solid solution films grown by reactive magnetron sputter epitaxy: Structural characterization and first-principles calculations," *J. Appl. Phys.*, vol. 107, no. 12, p. 123515, 2010.
- [15] M. A. Caro *et al.*, "Piezoelectric coefficients and spontaneous polarization of ScAlN," *J. Phys. Condens. Matter*, vol. 27, no. 24, p. 245901, 2015.
- [16] S. Manna *et al.*, "Enhanced piezoelectric response of AlN via CrN alloying," *Phys. Rev. Appl.*, vol. 9, no. 3, p. 034026, 2018.
- [17] O. Zywitzki, T. Modes, S. Barth, H. Bartzsch, and P. Frach, "Effect of scandium content on structure and piezoelectric properties of AlScN films deposited by reactive pulse magnetron sputtering," *Surf. Coat. Technol.*, vol. 309, pp. 417–422, Jan. 2017.
- [18] A. Žukauskaitė, E. Broitman, P. Sandström, L. Hultman, and J. Birch, "Nanoprobe mechanical and piezoelectric characterization of $\text{Sc}_x\text{Al}_{1-x}\text{N}$ (0001) thin films," *Phys. Status Solidi A*, vol. 212, no. 3, pp. 666–673, 2015.
- [19] S. Zhang, W. Y. Fu, D. Holec, C. J. Humphreys, and M. A. Moram, "Elastic constants and critical thicknesses of ScGaN and ScAlN," *J. Appl. Phys.*, vol. 114, no. 24, p. 243516, 2013.
- [20] K. E. Petersen and C. R. Guarnieri, "Young's modulus measurements of thin films using micromechanics," *J. Appl. Phys.*, vol. 50, no. 11, pp. 6761–6766, 1979.
- [21] L. Kiesewetter, J. M. Zhang, D. Houdeau, and A. Steckenborn, "Determination of Young's moduli of micromechanical thin films using the resonance method," *Sens. Actuators A, Phys.*, vol. 35, no. 2, pp. 153–159, 1992.
- [22] A. Ben Amar, M. Faucher, V. Brandli, Y. Cordier, and D. Théron, "Young's modulus extraction of epitaxial heterostructure AlGaN/GaN for MEMS application," *Phys. Status Solidi A*, vol. 211, no. 7, pp. 1655–1659, 2014.
- [23] E. Herth, E. Algré, J. Y. Rauch, J. C. Gerbedoen, N. Defrance, and P. Delobelle, "Modeling and characterization of piezoelectric beams based on an aluminum nitride thin-film layer," *Phys. Status Solidi A*, vol. 213, no. 1, pp. 114–121, 2016.
- [24] A. Andrei *et al.*, "AlN as an actuation material for MEMS applications: The case of AlN driven multilayered cantilevers," *Sens. Actuators A, Phys.*, vol. 141, no. 2, pp. 565–576, 2008.
- [25] S.-R. Jian, G.-J. Chen, J. S.-C. Jang, and Y.-S. Lai, "Nanomechanical properties of AlN(1 0 3) thin films by nanoindentation," *J. Alloys Compounds*, vol. 494, nos. 1–2, pp. 219–222, 2010.
- [26] S.-R. Jian, G.-J. Chen, and T.-C. Lin, "Berkovich nanoindentation on AlN thin films," *Nanosc. Res. Lett.*, vol. 5, no. 6, pp. 935–940, 2010.
- [27] P.-F. Yang, S.-R. Jian, S. Wu, Y.-S. Lai, C.-T. Wang, and R.-S. Chen, "Structural and mechanical characteristics of (1 0 3) AlN thin films prepared by radio frequency magnetron sputtering," *Appl. Surf. Sci.*, vol. 255, no. 11, pp. 5984–5988, 2009.
- [28] H. Li and J. J. Vlassak, "Determining the elastic modulus and hardness of an ultra-thin film on a substrate using nanoindentation," *J. Mater. Res.*, vol. 24, no. 3, pp. 1114–1126, 2009.
- [29] H. Y. Yu, S. C. Sanday, and B. B. Rath, "The effect of substrate on the elastic properties of films determined by the indentation test—Axisymmetric Boussinesq problem," *J. Mech. Phys. Solids*, vol. 38, no. 6, pp. 745–764, 1990.
- [30] A. Bikowski *et al.*, "Synthesis and characterization of (Sn,Zn)O alloys," *Chem. Mater.*, vol. 28, no. 21, pp. 7765–7772, 2016.
- [31] K. R. Talley *et al.*, "Implications of heterostructural alloying for enhanced piezoelectric performance of (Al,Sc)N," *Phys. Rev. Mater.*, vol. 2, no. 6, p. 63802, Jun. 2018.
- [32] X. Li and B. Bhushan, "A review of nanoindentation continuous stiffness measurement technique and its applications," *Mater. Characterization*, vol. 48, no. 1, pp. 11–36, 2002.
- [33] G. Kresse and D. Joubert, "From ultrasoft pseudopotentials to the projector augmented-wave method," *Phys. Rev. B, Condens. Matter*, vol. 59, no. 3, pp. 1758–1775, 1999.
- [34] G. Kresse and J. Furthmüller, "Efficiency of ab-initio total energy calculations for metals and semiconductors using a plane-wave basis set," *Comput. Mater. Sci.*, vol. 6, pp. 15–50, Jul. 1996.
- [35] J. P. Perdew, K. Burke, and M. Ernzerhof, "Generalized gradient approximation made simple," *Phys. Rev. Lett.*, vol. 77, pp. 3865–3868, Oct. 1996.
- [36] A. van de Walle *et al.*, "Efficient stochastic generation of special quasirandom structures," *Calphad*, vol. 42, pp. 13–18, Sep. 2013.
- [37] H. J. Monkhorst and J. D. Pack, "Special points for Brillouin-zone integrations," *Phys. Rev. B, Condens. Matter*, vol. 13, pp. 5188–5192, Jun. 1976.
- [38] B. Narayanan, I. E. Reimanis, E. R. Fuller, and C. V. Ciobanu, "Elastic constants of beta-eucryptite: A density functional theory study," *Phys. Rev. B, Condens. Matter*, vol. 81, no. 10, p. 104106, 2009.
- [39] J. F. Nye, *Physical Properties of Crystals, Their Representation by Tensors and Matrices*. London, U.K.: Oxford Univ. Press, 1985.
- [40] F. K. Lotgering, "Topotactical reactions with ferrimagnetic oxides having hexagonal crystal structures—I," *J. Inorganic Nucl. Chem.*, vol. 9, no. 2, pp. 113–123, 1959.
- [41] P. Haas, F. Tran, and P. Blaha, "Calculation of the lattice constant of solids with semilocal functionals," *Phys. Rev. B, Condens. Matter*, vol. 79, p. 085104, Feb. 2009.
- [42] R. D. Shannon, "Revised effective ionic radii and systematic studies of interatomic distances in halides and chalcogenides," *Acta Crystallogr. A, Found. Crystallogr.*, vol. 32, no. 5, pp. 751–767, 1976.
- [43] V. I. Razumovskiy, E. I. Isaev, A. V. Ruban, and P. A. Korzhavyi, "Ab initio calculations of elastic properties of Pt–Sc alloys," *Intermetallics*, vol. 16, no. 8, pp. 982–986, 2008.
- [44] V. V. Bannikov, I. R. Shein, and A. L. Ivanovskii, "Elastic and electronic properties of hexagonal rhenium sub-nitrides Re_3N and Re_2N in comparison with hcp-Re and wurtzite-like rhenium mononitride ReN ," *Phys. Status Solidi B*, vol. 248, no. 6, pp. 1369–1374, 2011.
- [45] C. E. Ekuma, D. Bagayoko, M. Jarrell, and J. Moreno, "Electronic, structural, and elastic properties of metal nitrides XN ($\text{X}=\text{Sc}$, Y): A first principle study," *AIP Adv.*, vol. 2, no. 3, p. 032163, 2012.
- [46] A. Delafargue and F.-J. Ulm, "Explicit approximations of the indentation modulus of elastically orthotropic solids for conical indenters," *Int. J. Solids Struct.*, vol. 41, no. 26, pp. 7351–7360, 2004.
- [47] R. Hill, "The elastic behaviour of a crystalline aggregate," *Proc. Phys. Soc. A*, vol. 65, no. 5, pp. 349–354, 1952.
- [48] J. J. Gilman, *Electronic Basis of the Strength of Materials*, 1st ed. Cambridge, U.K.: Cambridge Univ. Press, 2003.

- [49] M. Clement, L. Vergara, J. Sangrador, E. Iborra, and A. Sanz-Hervás, "SAW characteristics of AlN films sputtered on silicon substrates," *Ultrasonics*, vol. 42, nos. 1–9, pp. 403–407, 2004.
- [50] K.-S. Kao, C.-C. Cheng, and Y.-C. Chen, "Synthesis of C-axis-oriented aluminum nitride films by reactive RF magnetron sputtering for surface acoustic wave," *Jpn. J. Appl. Phys.*, vol. 40, no. 8, pp. 4969–4973, Aug. 2001.
- [51] V. Mortet *et al.*, "Surface acoustic wave propagation in aluminum nitride-unpolished freestanding diamond structures," *Appl. Phys. Lett.*, vol. 81, no. 9, pp. 1720–1722, Aug. 2002.
- [52] I. C. Oliveira, K. G. Grigorov, H. S. Maciel, M. Massi, and C. Otani, "High textured AlN thin films grown by RF magnetron sputtering: composition, structure, morphology and hardness," *Vacuum*, vol. 75, no. 4, pp. 331–338, 2004.
- [53] S.-H. Lee, K. H. Yoon, D.-S. Cheong, and J.-K. Lee, "Relationship between residual stress and structural properties of AlN films deposited by r.f. reactive sputtering," *Thin Solid Films*, vol. 435, nos. 1–2, pp. 193–198, Jul. 2003.
- [54] H. Y. Liu, G. S. Tang, F. Zeng, and F. Pan, "Influence of sputtering parameters on structures and residual stress of AlN films deposited by DC reactive magnetron sputtering at room temperature," *J. Cryst. Growth*, vol. 363, pp. 80–85, Jan. 2013.
- [55] V. Mortet *et al.*, "Surface acoustic wave propagation in aluminum nitride-unpolished freestanding diamond structures," *Appl. Phys. Lett.*, vol. 81, no. 9, pp. 1720–1722, Aug. 2002.
- [56] S.-H. Lee, K. H. Yoon, D.-S. Cheong, and J.-K. Lee, "Relationship between residual stress and structural properties of AlN films deposited by r.f. reactive sputtering," *Thin Solid Films*, vol. 435, nos. 1–2, pp. 193–198, Jul. 2003.
- [57] H. Y. Liu, G. S. Tang, F. Zeng, and F. Pan, "Influence of sputtering parameters on structures and residual stress of AlN films deposited by DC reactive magnetron sputtering at room temperature," *J. Cryst. Growth*, vol. 363, pp. 80–85, Jan. 2013.
- [58] F. Tasnádi *et al.*, "Origin of the anomalous piezoelectric response in wurtzite $\text{Sc}_x\text{Al}_{1-x}\text{N}$ alloys," *Phys. Rev. Lett.*, vol. 104, no. 13, p. 137601, 2010.



Dong Wu received the bachelor's degree in materials science and engineering from the Huazhong University of Science and Technology, Wuhan, China, in 2007, the master's degree in materials science from the Shanghai Institute of Optics and Fine Mechanics, Shanghai, China, in 2010, and the Ph.D. degree in materials science in 2015.

He has been devoted to the research of piezoelectric thin film at Colorado School of Mines since January 2016. He is currently a Field Process Engineer with Lam Research, Wuhan, China, focusing on evaluation and control of plasma etching in semiconductor industry.



Yachao Chen received the bachelor's degree in materials science and engineering from the Dalian University of Technology China, Dalian, China, in 2008, and the Ph.D. degree in materials science from the Colorado School of Mines, Golden, CO, USA, in 2017.

She is currently a Post-Doctoral Fellow with the Colorado School of Mines. Her research focuses on investigating the mechanical and electrical properties of novel piezoelectric thin films.

Dr. Chen received the Graduate Excellent in Materials Science Award in 2014.



Sukriti Manna received the B.E. degree in metallurgy from Jadavpur University, Kolkata, India, and the master's degree in materials engineering from the Indian Institute of Science, Bengaluru, India, where he focused on the development of a phase field model to study the evolution of microstructure in nickel-based super alloys. He is currently pursuing the Ph.D. degree in mechanical engineering with the Colorado School of Mines (CSM), Golden, CO, USA.

He joined CSM in 2014, and worked on pressure-induced phase transformation in lithium aluminum silicates (LAS). Currently, his work focuses on design and discovery of new high-performance piezoelectric materials relevant across all use scenarios with an initial focus on nitride alloys using first-principle calculations.

Kevin Talley, photograph and biography not available at the time of publication.



Andriy Zakutayev received the B.S. degree in electronics from Lviv Polytechnic National University, Lviv, Ukraine, in 2006, and the Ph.D. degree in physics from Oregon State University, Corvallis, OR, USA, in 2010, where he studied mixed-anion p-type transparent conductors.

He is currently a Scientist with the National Renewable Energy Laboratory, Golden, CO, USA. He is currently interested in the development of next-generation materials for advanced energy technologies, including solar cells, Li-ion batteries, piezoelectric devices, and fuel cells. To achieve these goals, he applies high-throughput experimental methods, in close iterative coupling with first-principles calculation.

Dr. Zakutayev was a recipient of the EMRS Young Scientist Award and other professional recognition.



Geoff L. Brennecka received the B.S. and M.S. degrees in ceramic engineering from the Missouri University of Science and Technology, Rolla, MO, USA, in 2001 and 2002, respectively, and the Ph.D. degree in materials science and engineering from the University of Illinois at Urbana-Champaign, Champaign, IL, USA, in 2006.

From 2006 to 2014, he was a member of the Technical Staff with Sandia National Laboratories. In 2014, he joined the Metallurgical and Materials Engineering Department, Colorado School of Mines, Golden, CO, USA, as an Assistant Professor, where he was promoted to an Associate Professor in 2018. His research focuses on the development and integration of electroceramic materials and devices.

Dr. Brennecka is a fellow of the American Ceramic Society (ACerS) and received a number of technical and service awards including the IEEE-UFFC Ferroelectrics Young Investigator Award in 2014 and a National Science Foundation Faculty Early Career Development CAREER Grant in 2016. He served the ACerS Board of Directors from 2014 to 2017 and the AdCom of the UFFC from 2015 to 2017.



Cristian V. Ciobanu received the B.Sc. degree in physics from the University of Bucharest, Bucharest, Romania, in 1995, and the M.Sc. and Ph.D. degrees in physics from Ohio State University, Columbus, OH, USA, in 1998 and 2001, respectively.

He is currently a Professor of mechanical engineering with the Colorado School of Mines, Golden, CO, USA. After a postdoctoral stage in the Division of Engineering, Brown University, Providence, RI, USA, he joined the Colorado School of Mines in 2004. He has coauthored over 80 refereed journal

articles, one book, and several chapters in edited books. His research interests are in nanoscale surface science, 2-D materials, piezoelectric ceramics, computational materials design, magnetic materials, optimization of atomic structures, and self-organized nanostructures on crystal surfaces, among others.

Dr. Ciobanu is a Lifetime Member of the American Physical Society and the Minerals, Metals, and Materials Society, and a fellow of the Institute of Physics (U.K.).



Corinne E. Packard received the Ph.D. degree in materials science and engineering from MIT, Cambridge, MA, USA.

She is currently an Associate Professor with the George S. Ansell Metallurgical and Materials Engineering Department, Colorado School of Mines, Golden, CO, USA. She holds a joint appointment at the National Renewable Energy Laboratory, National Center for Photovoltaics, Golden. She has over 30 archival publications, three issued patents, and 40 invited and contributed talks. Her research

program applies experimental techniques commonly used to characterize mechanical behavior and properties in structural materials to solve problems in ceramics in predominantly energy-related applications. She has focused on elucidating the principles and mechanisms of deformation behavior in ceramics at the microscale and nanoscale.

Dr. Packard received the National Science Foundation Faculty Early Career Development (CAREER) Award in 2014 and was selected as a TMS Young Leader. She received the AIME Robert Lansing Hardy Award in 2017.

Paul Constantine, photograph and biography not available at the time of publication.